This is a self-archived version of an original article. This version may differ from the original in pagination and typographic details.

Author(s): Chen, Zhonghua; Ristaniemi, Tapani; Cong, Fengyu; Wang, Hongkai

Title: Multi-resolution Statistical Shape Models for Multi-organ Shape Modelling

Please cite the original version:

Chen, Z., Ristaniemi, T., Cong, F., & Wang, H. (2020). Multi-resolution Statistical Shape Models for Multi-organ Shape Modelling. In M. Han, S. Qin, & N. Zhang (Eds.), ISNN 2020 : Advances in Neural Networks : 17th International Symposium on Neural Networks, Proceedings (pp. 74-84). Springer. Lecture Notes in Computer Science, 12557. https://doi.org/10.1007/978-3-030-64221-1_7

Multi-Resolution Statistical Shape Model for Multi-Organ Shape Modelling

Zhonghua Chen[1, 2], Tapani Ristaniemi[2], Fengyu Cong[1, 2], and Hongkai Wang[1 *]

[1]School of Biomedical Engineering, Faculty of Electronic Information and Electrical Engineering, Dalian University of Technology, Dalian 116024, China
`chenzh4693@foxmail.com, cong@dlut.edu.cn,`
`wang.hongkai@dlut.edu.cn`
[2]Faculty of Information Technology, University of Jyväskylä, Jyväskylä 40100, Finland
`tapani.e.ristaniemi@jyu.fi`

Abstract. Statistical shape models (SSMs) are widely used in medical image segmentation. However, traditional SSM methods suffer from the High-Dimension-Low-Sample-Size (HDLSS) problem in modelling. In this work, we extend the state-of-the-art multi-resultion SSM approach from two dimension (2D) to three dimension (3D) and from single organ to multiple organs. Then we proposed a multi-resolution multi-organ 3D SSM method that uses a downsampling-and-interpolation strategy to overcome HDLSS problem. We also use an inter-surface-point distance thresholding scheme to achieve multi-resolution modelling effect. Our method is tested on the modelling of multiple mouse abdominal organs from mouse micro-CT images in three different resolution levels, including multi-organ level, single organ level and local structure level. The minimum specificity error and generalization error of this method are less than 0.3 mm, which are close to the pixel resolution of mouse CT images (0.2 mm) and better than traditional principal component analysis (PCA) method.

Keywords: Multi-resolution multi-organ SSM, PCA, HDLSS, Mouse micro-CT image, Liver, Spleen, Left kidney, Right kidney, Geodesic distance, Euclidean distance.

1 Introduction

In the last three decades, SSM approaches have been used as one of the most important methods to segment and register organs for medical image analysis [4]. The applications of SSMs includes but not limit to the following fields: 1) Medical image segmentation and registration [2, 3, 7]. 2) Clinical diagnosis and treatment [1, 11]. 3) Analysis of organ contraction [10].

Due to the complexity of medical images, SSMs of 3D organs are playing an increasingly important role in medical image segmentation. To represent 3D organ shapes, landmarks are sampled from the organ surface. However, a challenging problem of 3D SSM construction is that the number of training samples is small while the

number of landmarks is large [12]. To fully capture the great variability of 3D shape, the traditional PCA modelling method needs to provide a large number of representative training samples to achieve a good modelling effect, which usually requires a lot of labor and is even impossible to complete. This problem is later called High-Dimension-Low-Sample-Size (HDLSS) problem, which leads to insufficient and inaccurate expression of the model.

In order to solve the HDLSS problem, Wilms et al. [16] proposed a multi-resolution statistical shape model with the traditional PCA method based on local distance constraints in 2017, and they used this method to construct a 2D multi-resolution SSM of human hand shape and cardiopulmonary shape. The method is an important extension of the traditional SSM method, which can be used to obtain statistical deformation models of objects at different resolution levels. In addition, it makes the resulting models achieve better generalization and specificity based on fewer training samples. However, one limitation of this method is that it takes up a lot of memory and is not suitable for cases where there are many sampling points. Therefore, Wilms et al. only modelled simple 2D shapes in their study. Unfortunately, the 3D shape vectors of multiple organs usually contain thousands or even tens of thousands of sampling points. Moreover, since multiple organ shape modelling usually requires more sampling points than single organ, this method is not applicable to multi-organ modelling as well. These drawbacks limit the application of this method to multi-organ 3D shape modelling.

In this article, we propose a solution to extend the multi-resolution SSM approach to 3D shape modelling of multiple organs with large number of surface points. Our methods combines 3D object surface downsampling with Laplace diffusion equation to construct multi-resolution multi-organ 3D SSM. We obtain deformation components in three resolution levels, which are the "multi-organ level", "single organ level" and "local structure level". The models obtained from the above three resolution levels are compared quantitatively with the traditional PCA modelling methods in terms of model generalization and specific performance, and we obtain better modelling performance than the traditional methods.

2   Materials and Methods

2.1   Description of Mouse Micro-CT Data

The multi-organ shape training samples of mouse micro-CT images are taken from the Molecular Imaging Centre of the University of California, Los Angeles [14, 15]. During the imaging process, mice are injected with liver contrast agent Fenestra LC (ART, Montreal, QC, Canada) for clear imaging of abdominal organs. The weights of the tested mice range from 15 to 30 grams, and the data are selected according to the following principles for modelling: (1) Boundaries of the abdominal organs of the mouse: livers, spleens, and kidneys are clear. (2) There are no motion artefacts in the CT images of mice. (3) There are no cases where the livers, spleens and kidneys of the mice deviate from the normal shape. Mice are imaged in a multi-mode indoor

prone position that provides anesthesia and heating [13]. Although the imaging room limits the possible postures of the mice, these postures are not strictly normalized. The random body bending postures in the left, right, and backward directions are included in the data set. The imaging system is MicroCAT II Small Animal CT (Siemens Preclinical Solutions, Knoxville, TN). Equipment acquisition parameters for imaging: exposure setting 70 kVp, 500 mAs, 500 ms and 360 step rotation, 2.0 mm aluminum filter. In the image acquisition process, an improved Feld Kamp process is used to reconstruct the image so that the isotropic voxel size is 0.2 mm, the image matrix size is $256 \times 256 \times 496$, and the pixel resolution is 0.2 mm.

In this study, 98 mouse micro-CT images are collected as training samples for model construction. Small animal imaging experts are invited to segment the 3D regions of livers, spleens, left kidneys, and right kidneys from the images, and then use the moving cube algorithm [6] to convert the segmented label maps to mesh surfaces. On this basis, one of the 98 sample surfaces is selected as the template surface, and the point cloud registration algorithm [8, 9] is used to register the template to all other training samples, so that different samples have the same number of mesh vertices, and each vertex corresponds to the same anatomical position in different samples, thus completing the preparation of all training data. Fig.1 illustrates the entire training data preparation process.
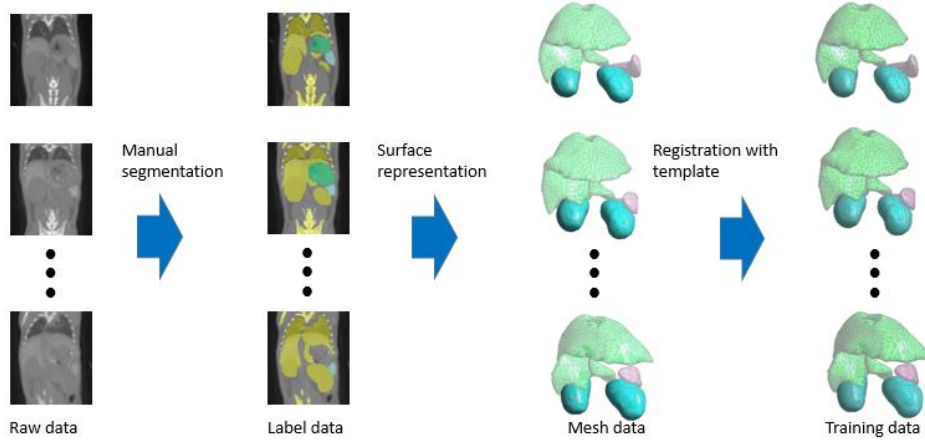

Fig. 1. The construction process for preparing the training data of the mouse multi-organ shape model

2.2 Description of Algorithms

The Construction of Multi-Resolution SSM.

1. Given N d (d = 3) dimensional mouse abdominal multi-organ training models $\{\mathbf{S_i}\}_1^N$, where $\mathbf{S_i} = \{\mathbf{X_{1,i}}, ..., \mathbf{X_{j,i}}, ..., \mathbf{X_{M,i}}\}$ contains M points, each point $\mathbf{X_{j,i}} = (x_{j,i}, y_{j,i}, z_{j,i})^T$ is distributed on the surface of the training model. Then calcu-

late the average model of the training models, the calculation formula is shown in formula (1):

$$\vec{\mu} = \frac{1}{N}\sum_{i=1}^{N} S_i \tag{1}$$

2. After normalization, the covariance matrix of the coordinates of different dimensional points is calculated, and the calculation formula is shown in formula (2):

$$C = \frac{1}{N-1}\sum_{i=1}^{N}(S_i - \vec{\mu})(S_i - \vec{\mu})^T \tag{2}$$

3. Calculate the point-to-point geodesic distance $d_{geo}(X_i, X_j)$ on each model surface, and use rule (3) to set the values of the two sides of the covariance matrix C symmetrical to 0:

$$\rho_{i,j} = \begin{cases} \frac{\text{cov}(X_i,X_j)}{\sigma_i\sigma_j} & \text{if } d_{geo}(X_i, X_j) \leq \tau \\ 0 & \text{else} \end{cases} \tag{3}$$

where σ_i and σ_j are the standard deviations of the i-th and j-th dimensions, respectively, and τ is the threshold given in the experiment according to the relevant rules, so that a simplified symmetric matrix $R_1 = \begin{pmatrix} \rho_{1,1} & \cdots & \rho_{1,M} \\ \vdots & \ddots & \vdots \\ \rho_{M,1} & \cdots & \rho_{M,M} \end{pmatrix}$.

4. Since R_1 is not positive semi-definite and cannot be implemented eigenvalue decomposition, it is necessary to use the approximation method [5] to find an approximate positive semi-definite matrix R_2 replacing R_1 with formula (4):

$$R_2 = \min_{A}\|A - R_1\|_F$$

$$\det(A) \geq 0 \tag{4}$$

$$\text{diag}(A) = 1$$

5. Calculate the eigenvector matrix U_τ of R_2 and the corresponding eigenvalue matrix Λ_τ, as shown in formula (5):

$$\begin{pmatrix} \sigma_1 & \cdots & 0 \\ \vdots & \ddots & \vdots \\ 0 & \cdots & \sigma_{dM} \end{pmatrix} R_2 \begin{pmatrix} \sigma_1 & \cdots & 0 \\ \vdots & \ddots & \vdots \\ 0 & \cdots & \sigma_{dM} \end{pmatrix} = U_\tau \Lambda_\tau U_\tau^T \tag{5}$$

where the eigenvector set included in U_τ is represented as P, and the eigenvalue vector on the diagonal of Λ_τ is represented as $\vec{\lambda}$.

6. When different values of distance threshold τ are selected in equation (3), the model will show different deformation capabilities locally; when $\tau \geq \max_{i,j} d_{geo}(\vec{x}_i, \vec{y}_i)$, the constructed model is the traditional SSM; when $\tau = 0$, the physical coordinate points on all training samples lose their relevance, and the constructed model cannot be deformed, which has no practical significance. By defining a series of thresholds $\tau_1 > \tau_2 > \cdots > \tau_L$, a multi-resolution scheme is defined to obtain a set of shape models $\{\vec{\mu}, P_1, \dots, P_L, \vec{\lambda}_1, \dots, \vec{\lambda}_L\}$ that vary from global to local. However, these models are highly dependent and redundant, and do not constitute a single shape space. Therefore, it is necessary to retain global information to combine

them into a subspace, so that the feature vectors provided by the local SSM can optimally represent more local information. Based on step 1 to 5, the algorithm for constructing a multi-resolution shape model is derived as follows:

Suppose that there are N training model data matrices $\mathbf{X} = (\overrightarrow{\mathbf{s_1}} \,|\, \overrightarrow{\mathbf{s_2}} \cdots \,|\, \overrightarrow{\mathbf{s_N}}) \epsilon \mathbf{R}^{m \times N}$, the thresholds of geodesic distance on each model surface are $\boldsymbol{\tau_1} > \boldsymbol{\tau_2} > \cdots > \boldsymbol{\tau_L}$. Calculate the average model $\vec{\boldsymbol{\mu}} = \frac{1}{N} \sum_{i=1}^{N} \overrightarrow{\mathbf{s_i}}$ of the training models. And define the distance matrix d_{geo} on the average model. Assuming that the iteration index r ranges from 1 to L in the calculation process, where r represents the number of models, the deformation coefficient of the local SSM is defined as $\overrightarrow{\lambda_{\tau_r}}$, and the deformation component corresponding to the coefficient is defined as $\mathbf{P}_{\tau_r}$.

When $r = 1$, it means that there is only one shape model space, and the multi-organ statistical shape model can be obtained by directly using the traditional PCA method; when $r > 1$, it means that there are multiple shape model spaces, and these model spaces need to be combined for singular value decomposition. The decomposition process is as follows:

$$\mathbf{U}(\cos\theta)\mathbf{V}^{\mathbf{T}} \leftarrow \text{svd}(\mathbf{P}_{\mathbf{MR}}^{\mathbf{T}} \mathbf{P}_{\tau_r}) \tag{6}$$

$$\mathbf{S} = \begin{pmatrix} \cos\theta_{\mathbf{k}\times\mathbf{k}} & \cdots & 0 \\ \vdots & \cdot & \vdots \\ 0 & \cdots & \mathbf{I}_{(\mathbf{l}-\mathbf{k})\times(\mathbf{l}-\mathbf{k})} \end{pmatrix} \tag{7}$$

where svd() represents singular value decomposition and calculates the transform base $\hat{\mathbf{B}}$, $\hat{\mathbf{B}} = \mathbf{P}_{\tau_r}\mathbf{V}\mathbf{S}^{\mathbf{T}}$. Then, calculate the covariance matrix after spatial transformation:

$$\hat{\boldsymbol{\Sigma}}_{\tau_{MR}} = \left(\sigma_{i,j}^{\tau_{MR}}\right) = \mathbf{U}^{\mathbf{T}} \begin{pmatrix} \lambda_{\tau_{MR},1} & \cdots & 0 \\ \vdots & \ddots & \vdots \\ 0 & \cdots & \lambda_{\tau_{MR},k} \end{pmatrix} \mathbf{U} \tag{8}$$

$$\hat{\boldsymbol{\Sigma}}_{\tau_r} = \left(\sigma_{i,j}^{\tau_r}\right) = \mathbf{V}^{\mathbf{T}} \begin{pmatrix} \lambda_{\tau_r,1} & \cdots & 0 \\ \vdots & \ddots & \vdots \\ 0 & \cdots & \lambda_{\tau_r,l} \end{pmatrix} \mathbf{V} \tag{9}$$

$\hat{\boldsymbol{\Sigma}}_{MR,r} = (\sigma_{i,j}^{\tau_{MR},\tau_r})$, where $\sigma_{i,j}^{\tau_{MR},\tau_r} = \begin{cases} \sigma_{i,j}^{\tau_{MR}} & \text{if } i,j \in [1,k] \\ \sigma_{i,j}^{\tau_r} & \text{if } i,j \in [k+1,l] \\ 0 & \text{else} \end{cases}$, finally calculate the uncorrelated basis vectors and the corresponding feature values:

$$[P_{MR}, \hat{\lambda}_{MR}] \leftarrow \text{eig}(\hat{\mathbf{B}}\hat{\boldsymbol{\Sigma}}_{MR,r}\hat{\mathbf{B}}^{\mathbf{T}}) \tag{10}$$

where eig() represents eigenvalue decomposition. And the multi-resolution multi-organ SSM $\boldsymbol{\mu}$ is represented as follows:

$$\boldsymbol{\mu} = \vec{\boldsymbol{\mu}} + \hat{\lambda}_{MR}P_{MR} \tag{11}$$

Multi-Resolution Multi-Organ SSM.

In order to extend this method to the construction of 3D multi-organ models with a large number of sample points, the idea adopted in this study is to first downsample the vertices on the model surface. Then we extend the method of Wilms et al. to train the down-sampled 3D point sets to obtain a multi-resolution model shape. Finally, we interpolate the deformation vectors of the down-sampled vertices to generate deformation vectors of all vertices on the entire surface.

Fig.2 shows the idea of this improved method, where Fig.2 (a) shows the down-sampled vertices (marked in red) on the surface of the organ. There are a total of 3759 vertices in four kinds of organs (livers, spleens, left kidneys, right kidneys) in this study, and 375 vertices are obtained after 10 times down sampling, which can be used to construct a model in a computer with 16G memory. Fig.2 (b) shows the deformation vectors (represented by black arrows) on the down-sampled vertices of this model, and Fig.2 (c) shows the deformation vectors on all vertices by interpolating the deformation vectors of down-sampled vertices over the entire model surface, The interpolation method used is the Laplace iteration diffusion algorithm of the surface:

$$\vec{X}_{i_{(n+1)}} = \vec{X}_{i_n} + \frac{\lambda}{M}\sum_{j=0}^{M}(\vec{X}_{j_n} - \vec{X}_{i_n}) \tag{12}$$

where n represents the number of iterations, i is the vertex index, $\vec{x}_{i_n}$ represents the deformation vector of the i-th vertex coordinate at the n-th iteration, $j = 0,1,\ldots,M$ represents $M+1$ indexes of neighbor vertices around vertex i, λ represents the smooth intensity coefficient. At the beginning of the iteration ($n = 0$), first set the deformation vector $\vec{x}_{i_0}$ of the down-sampled vertices to the modeled feature vector P_{MR}, and set the deformation vector of the other vertices to 0; during the iteration process, keep the deformation vectors of down-sampled vertices always to be P_{MR}, and the deformation vectors of other vertices are calculated by formula (12). In order to obtain the desirable interpolation effect, through repeated testing, the maximum number of iterations is set to 1000, and the value of λ is set to 0.8. It can be seen from Fig.2 (c) that after interpolation, the deformation vectors on a small number of down-sampled points smoothly spread to the entire model surface. According to this method, the whole deformation components of the shape model are obtained by interpolating all vertices on the model surface, and the overall deformation of the model is further realized according to the interpolation results. It should be noted that although the deformation vectors are obtained by interpolation instead of by training all vertices, in the case of limited memory, this method can obtain reasonable deformation vectors for a large number of vertices of multiple organs. After observation and quantitative measurement (see this in Results section), the modelling results are better than the traditional global shape model.

In addition to the interpolation algorithm described above, the selection of the resolution in Wilms et al. method is also improved in this study to make it more applicable to multiple organs. Because the original algorithm of Wilms et al. did not specifically consider the problem of modelling multiple organs, but only imposed geodesic distance constraints on the range of the local deformation to generate multi-resolution models under different distance constraints. However, in the case of multi-

organ modelling, a simple geodesic distance cannot properly describe the distance relationship between two points belonging to different organs. For example, if the Euclidean distance between a point at the bottom of a lung and another point at the top of the liver is very close, these two points should have strong correlation in terms of common deformation because of the bottom of the lung and the top of the liver always coincide with each other. But according to the principle of the geodesic distance constraint in the Wilms et al. Algorithm, these two points belong to different organs, and the geodesic distance will be farther, so that the correlation between them in a model becomes smaller and does not meet the deformation regulation of adjacent organs. Based on the above considerations, this study uses Euclidean distance instead of geodesic distance as a constraint. The approach is as follows:

Based on the local deformed multi-organ SSM constructed in steps 1 to 6, the distances of surface vertices are calculated by combining the modified Euclidean distance between different organs with the geodesic distance expressed in equation (3). This article specifies that the geodesic distance of points on different organ models is infinite, and the Euclidean distance of points on different organ models can be calculated. Given a model vector $\vec{s}$ containing O target calibration points, and $\vec{s} = \left(\vec{x}_{1,1}^T, \ldots, \vec{x}_{1,M_1}^T, \vec{x}_{2,1}^T, \ldots, \vec{x}_{2,M_2}^T, \ldots, \vec{x}_{O,1}^T, \ldots, \vec{x}_{O,M_O}^T\right)^T$, where M_i represents the number of landmarks of the i-th model, $i \in \{1, \ldots, O\}$. Define the undirected graph $G_g(V, E_g)$, $V = \left\{\vec{x}_{i,j} \,\middle|\, i \in \{1, \ldots, O\}, j \in \{1, \ldots, M_i\}\right\}$ represents the vertices of the undirected graph, $E_g = \left\{\left(\vec{x}_{i,j}, \vec{x}_{i,k}\right) \middle| i \in \{1, \ldots, O\}, j \in \{1, \ldots, M_i\}, k \in N(\vec{x}_{i,j})\right\}$, $N(\vec{x}_{i,j})$ is the direct neighbourhood of point $\vec{x}_{i,j}$ on target i. The weight $w_{i,j,k}^g$ of edge $\left(\vec{x}_{i,j}, \vec{x}_{i,k}\right)$ is represented by the Euclidean distance between two points:

$$w_{i,j,k}^g = \left\|\vec{x}_{i,j} - \vec{x}_{i,k}\right\| \tag{13}$$

The geodesic distance $d_{geo}(\vec{x}, \vec{y})$ between two points on the target surface can be estimated by the shortest path in G_g. There is no connection relationship between different targets in G_g, so the distance between points on different targets is infinite.

Define the second fully connected undirected graph $G_e(V, E_e)$, and the edge weights represent the Euclidean distances of the scaled translation:

$$w_{i,j,l,k}^e = \eta\left\|\vec{x}_{i,j} - \vec{x}_{i,k}\right\| + \delta, \quad \eta, \delta \epsilon R \tag{14}$$

Use $d_e(\vec{x}, \vec{y})$, $\vec{x}, \vec{y} \in V$ represents the shortest distance in G_e. Combine equation (13) with (14), It can be seen from the two equations that on the same target, when $\eta \leq 1, \delta = 0$, $d_e(\vec{x}, \vec{y}) \leq d_{geo}(\vec{x}, \vec{y})$; when $\eta \geq 1, \delta \geq \max[d_{geo}\left(\vec{x}_{i,j}, \vec{x}_{i,k}\right)]$, $d_e(\vec{x}, \vec{y}) > d_{geo}(\vec{x}, \vec{y})$. On the same target surface, assumed that the energy required from point $\vec{x}$ to point $\vec{y}$ is equal to $d_{geo}(\vec{x}, \vec{y})$, and the coefficient η represents the energy ratio of moving the same distance in the embedding space R^d, which also means the relative viscosity of the space, δ represents the energy required to overcome the adhesion force to leave the target surface. No matter moving on the target surface or moving in the embedding space, the merged distance $d(\vec{x}, \vec{y})$ of two points $\vec{x}, \vec{y}$ in V is a path with minimum energy. Therefore, the shortest path $d(\vec{x}, \vec{y})$ of the combined fully connected graph $G(V, E)$ can be obtained with edge weights equation (15):

$$w_{i,j,l,k} = \begin{cases} \min\left(w_{i,j,k}^{g}, w_{i,j,l,k}^{e}\right) & \text{if } \left(\vec{x}_{i,j}, \vec{x}_{l,k}\right) \in E_e \\ w_{i,j,l,k}^{e} & \text{else} \end{cases} \tag{15}$$

We set the ratio σ of the distance threshold τ to 0.99 and 0.5 respectively, and we can get two shape models with different resolutions. Since the geodesic distance between organs is defined as infinity, $\sigma = 0.99$ retains the deformation of a single organ very well, and each deformation component in the obtained model corresponds to a certain deformation mode of a single organ. On the other hand, based on the definition of Euclidean distance, when $\sigma = 0.5$, the common deformation between vertices is limited to local areas of the organ, and the deformation components of the obtained model correspond to deformation modes of the local area of the organ.

In summary, we combine the traditional global model ($\sigma = 1$, the traditional PCA modeling method), the single organ level model ($\sigma = 0.99$) and the local organ level model ($\sigma = 0.5$) with formulas (6)-(11). A 3D SSM based on prior knowledge is obtained which is suitable for modelling multiple organs, and the deformation components contained in this model divided into three resolution levels, that is, global level(multi-organ level), single organ level and local structure level. This modelling method well reflects the different levels of deformation in a multi-organ combination system and describes the deformation of multiple organs better than traditional global models.
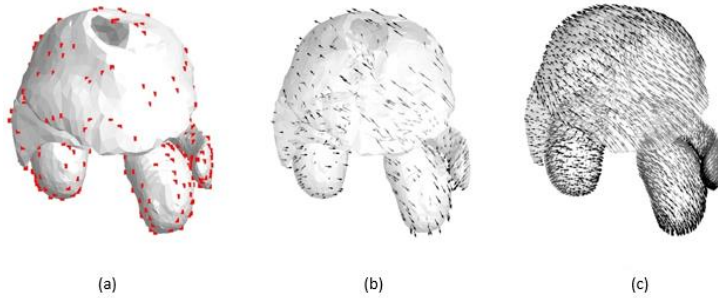

Fig. 2. Schematic diagram of improved method based on downsampling training and deformation vectors interpolation. (a) Down-sampled vertices; (b) Deformation of the down-sampled vertices; (c) The interpolated deformation vectors of all vertices on the surface.

3   Results

Fig.3 shows the modelling effect of the deformation components of the multi-resolution multi-organ shape model constructed by the method in this article. Due to the limited space of this article, the model of each resolution level only shows the results of the first three deformation components on the average shape model. Deformation components are denoted by PC_1, PC_2 and PC_3, respectively. $\lambda_1, \lambda_2, \lambda_3$ are the corresponding eigenvalues, and α_1, α_2, α_3, the shape coefficients of the multi-resolution multi-organ SSM, are set as the weights of model deformation. For each

resolution level, the first row show the average models (the average models of the three resolution levels are the same), and the second to fourth rows show the deformation results of the average model with the first three deformation components. Fig. 3 (a), 3 (b) and 3 (c) show the different shapes when the shape coefficient of a component takes different values, and the parts with obvious deformation are circled in the right column. From Fig.3 (a), we can see that the organ deformations reflected by different components all occur together among multiple organs. For example, PC_1 reflects the change in the distance between the left lower lobe of the liver and the spleen, which is most likely caused by the size change of the stomach between them. PC_2 reflects the closeness between the anterior half of the spleen and the left kidney, and PC_3 reflects the change in the distance between the liver and the two kidneys. Fig.3 (b) reflects the deformation of a single organ level, in which PC_1, PC_2 and PC_3 correspond to the deformation of the livers, left kidneys and spleens, respectively. Fig.3 (c) Reflects the local deformation of each organ, such as PC_1 reflects the deformation of the left lower lobe of the liver, PC_2 reflects the deformation of the anterior half of the spleen, PC_3 reflects changes in the anterior curvature of the right kidney. When local deformation is performed, other parts of the same organ keep unchanged. These results show that the method in this study can effectively model the deformation of organs at different resolution levels.

In addition to the above qualitative observation of model deformation modes, two quantitative indicators of generalization and specificity [4] are also used to evaluate the accuracy of model construction in the study.

The generalization of the model is used to measure the model's ability to represent new shapes (that is, shapes not included in the training samples). Generalization can be measured by using Leave-One-Out (LOO) method: assuming there are N training samples, one sample is left as the test sample S_j, and the other $N-1$ samples $\{S_i | i = 1,2,\dots,N, i \neq j\}$ are used to train the model $\mathbf{M}^*$, and then fit S_j through the deformation of $\mathbf{M}^*$, and calculate the average distance between the fitting result and S_j as the fitting error e_j. This process is repeated N times (ie j=1,2,...,N), and then set the average error $e_g = \frac{\sum_{j=1}^{N} e_j}{N}$ of N times as a measure of model generalization ability, the smaller the value of e_g is, the better the model generalization ability is.

The specificity of the model is used to measure the model's ability to represent its own training samples. The specificity of the SSM can be tested by randomly generating shape samples: when we get the model based on N training samples, the shape coefficient vectors $\{\vec{\alpha}_j | j = 1,2,\dots,K\}$ of K group models is randomly generated based on the normal distribution, where the mean value of the normal distribution is 0, and the standard deviation is the standard deviation obtained by eigenvalue decomposition of PCA method. Based on each randomly generated coefficient $\vec{\alpha}_j$, generate its corresponding 3D shape, and find a sample whose surface distance is closest to this shape in the training sample set, and set this surface distance as the error e_j of the jth random sample. Then calculate the average error $e_s = \frac{\sum_{j=1}^{K} e_j}{K}$ of K random samples as a measure of model specificity, the smaller the value of e_s is, the better the model specificity ability is.
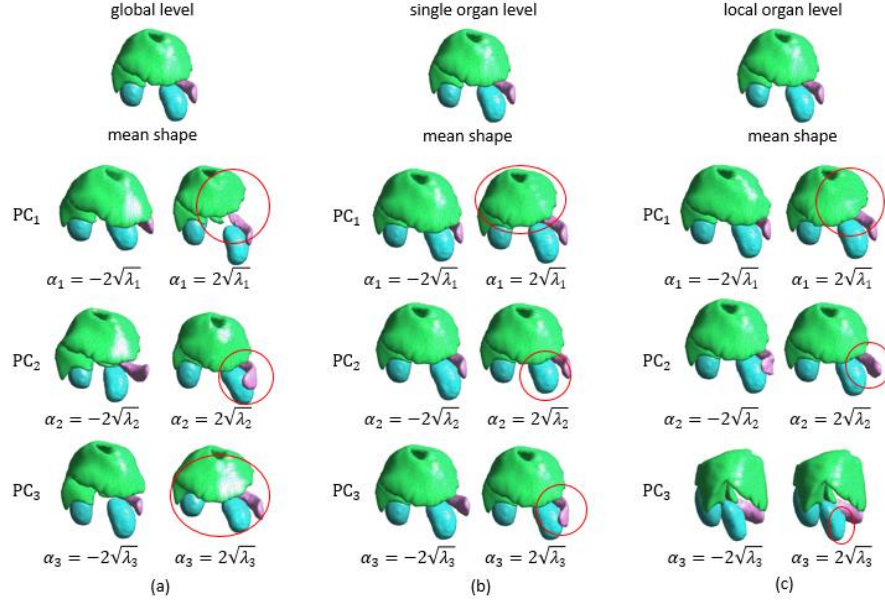
Fig. 3. Deformation components in multi-resolution multi-statistical shape model. (a) Deformation components at the global resolution level; (b) Deformation components at the single-organ resolution level; (c) Deformation components at the local structure level of the organ.
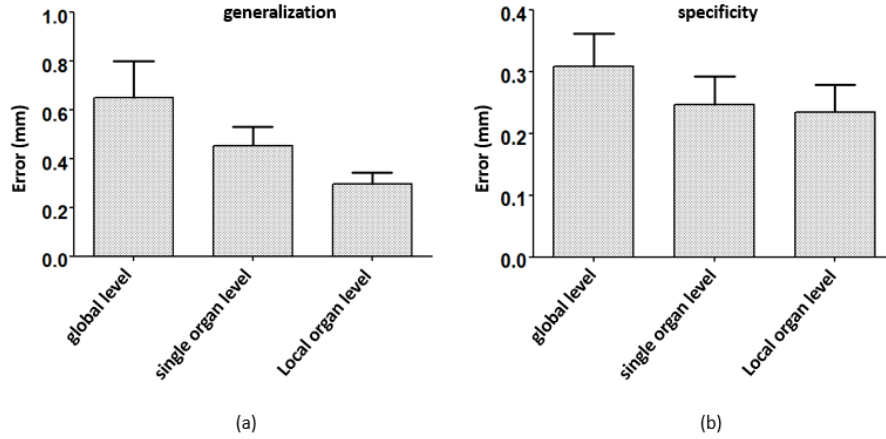

Fig. 4. Quantitative performance evaluation of multi-resolution multi-organ model (a) Generalization error; (b) Specificity error

In order to reflect the improvement effect of the multi-resolution model on the generalization error e_g and the specificity error e_s, this experiment calculates the results of e_g and e_s at different resolution levels, as shown in Fig.4. Both for generalization error and specificity error, the mean value and standard deviation of the three

model errors from global resolution level to local structure resolution level are within 1.0 mm. When the model changes from global level to local structure level, the mean value and variance of the errors are gradually decreasing, which indicates that the multi-organ model with local structure level is more accurate for the boundary registration. This means that the multi-resolution multi-organ model constructed in this paper has better generalization and specificity than the global model constructed by traditional PCA method. Encouragingly, even for generalization errors, the minimum mean value of the multi-resolution multi-organ model has reached about 0.3 mm, which is close to the minimum mean value of the specificity error of 0.25 mm. More importantly, it is also close to the pixel resolution of mouse CT images of 0.2 mm, and is lower than the average specificity error of the traditional global model of 0.31 mm.

4   Conclusion

This article proposes a multi-resolution multi-organ shape prior knowledge model construction method and uses it to model multiple abdominal organs of mouse micro-CT images. Compared to the recently proposed state-of-the-art 2D multi-resolution SSM method by Wilms et al., our method solves the shortcomings of memory occupation and thus extend the method to 3D space. On the other hand, this work extend the method to multi-organ modelling and can be used for modelling the inter-subject shape changes of multi-organ, single organ and local structure levels. This method surpasses the traditional PCA modelling method in terms of both generalization and specificity. It should be pointed out that although this work builds a model based on the abdominal organs of mouse, the method in this study is also applicable to the multi-organ modelling of human or other animal bodies. The model constructed in this work lays the foundation of shape prior knowledge for further multi-organ image segmentation.

Acknowledgements

References

1. BONDIAU, P.Y. and MALANDAIN, G., 1997. Eye reconstruction and CT-retinography fusion for proton treatment planning of ocular diseases. In CVRMed-MRCAS'97, J.

TROCCAZ, E. GRIMSON and R. MÖSGES Eds. Springer Berlin Heidelberg, Berlin, Heidelberg, 705-714.

2. COOTES, T.F., EDWARDS, G.J., and TAYLOR, C.J., 2001. Active appearance models. IEEE Transactions on Pattern Analysis and Machine Intelligence 23, 6, 681-685.

3. COOTES, T.F., TAYLOR, C.J., COOPER, D.H., and GRAHAM, J., 1995. Active Shape Models-Their Training and Application. Computer Vision and Image Understanding 61, 1 (1995/01/01/), 38-59.

4. HEIMANN, T. and MEINZER, H.-P., 2009. Statistical shape models for 3D medical image segmentation: A review. Medical Image Analysis 13, 4 (2009/08/01/), 543-563.

5. HIGHAM, N.J., 2002. Computing the nearest correlation matrix—a problem from finance. IMA Journal of Numerical Analysis 22, 3, 329-343.

6. LORENSEN, W. and CLINE, H., 1987. Marching Cubes: A High Resolution 3D Surface Construction Algorithm. ACM SIGGRAPH Computer Graphics 21(08/01), 163.

7. LORENZ, C. and KRAHNSTOVER, N., 1999. 3D statistical shape models for medical image segmentation. In Second International Conference on 3-D Digital Imaging and Modeling (Cat. No.PR00062), 414-423.

8. MARANI, R., RENÒ, V., NITTI, M., D'ORAZIO, T., and STELLA, E., 2016. A Modified Iterative Closest Point Algorithm for 3D Point Cloud Registration. Computer-Aided Civil and Infrastructure Engineering 31, 7 (2016/07/01), 515-534.

9. PARK, S. and LIM, S.-J., 2014. Template-Based Reconstruction of Surface Mesh Animation from Point Cloud Animation. ETRI Journal 36(12/01), 1008-1015.

10. RUECKERT, D. and BURGER, P., 1997. Shape-based segmentation and tracking in 4D cardiac MR images. In CVRMed-MRCAS'97, J. TROCCAZ, E. GRIMSON and R. MÖSGES Eds. Springer Berlin Heidelberg, Berlin, Heidelberg, 43-52.

11. SANDOR, S. and LEAHY, R., 1997. Surface-based labeling of cortical anatomy using a deformable atlas. IEEE Transactions on Medical Imaging 16, 1, 41-54.

12. STEGMANN, M. and GOMEZ, D., 2002. A Brief Introduction to Statistical Shape Analysis. Informatics and Mathematical Modelling, Technical University of Denmark, DTU 15(01/01).

13. SUCKOW, C., KUNTNER, C., CHOW, P., SILVERMAN, R., CHATZIIOANNOU, A., and STOUT, D., 2009. Multimodality Rodent Imaging Chambers for Use Under Barrier Conditions with Gas Anesthesia. Molecular Imaging and Biology 11, 2 (2009/03/01), 100-106.

14. SUCKOW, C.E. and STOUT, D.B., 2008. MicroCT Liver Contrast Agent Enhancement Over Time, Dose, and Mouse Strain. Molecular Imaging and Biology 10, 2 (2008/03/01), 114-120.

15. WANG, H., STOUT, D.B., and CHATZIIOANNOU, A.F., 2012. Estimation of Mouse Organ Locations Through Registration of a Statistical Mouse Atlas With Micro-CT Images. IEEE Transactions on Medical Imaging 31, 1, 88-102.

16. WILMS, M., HANDELS, H., and EHRHARDT, J., 2017. Multi-resolution multi-object statistical shape models based on the locality assumption. Medical Image Analysis 38 (02/01).